Inflatable Aerocapture Decelerators for Mars Orbiters

Glen J. Brown*
Vertigo, Inc., Santa Cruz, California 95060

and

J. Stephen Lingard†, Matthew G. Darley‡ and John C. Underwood§
Vorticity Ltd, Chalgrove, Oxfordshire, OX44 7RW, United Kingdom

A multi-disciplinary research program was recently completed, sponsored by NASA Marshall Space Flight Center, on the subject of aerocapture of spacecraft weighing up to 5 metric tons at Mars. Heavier spacecraft will require deployable drag area beyond the dimensional limits of current and planned launch fairings. This research focuses on the approach of lightweight inflatable decelerators constructed with thin films, using fiber reinforcement and having a temperature limitation of 500 °C. Trajectory analysis defines trajectories for a range of low ballistic coefficients for which convective heat flux is compatible with the material set. Fluid-Structure Interaction (FSI) tools are expanded to include the rarified flow regime. Several non-symmetrical configurations are evaluated for their capability to develop lift as part of the necessary trajectory control strategy. Manufacturing technology is developed for 3-D stretch forming of polyimide films and for tailored fiber reinforcement of thin films. Finally, the mass of the decelerator is estimated and compared to the mass of a traditional rigid aeroshell.

Nomenclature

β	=	ballistic coefficient
C_D	=	drag coefficient
C_P	=	pressure coefficient
D	=	reference diameter
DSMC	=	Direct Simulation Monte Carlo
FPA	=	flight path angle
L/D	=	lift-to-drag ratio
MFP	=	mean free path (hard sphere)
ρ	=	atmospheric density
q	=	dynamic pressure
s	=	surface distance from center of capsule
TPS	=	thermal protection system
V	=	free stream velocity

I. Introduction

INFLATABLE aerodynamic decelerators are needed when a spacecraft requires a larger aerodynamic area than will fit within a launch fairing. Today that limitation is generally accepted to be 5 m. diameter. Decelerators for entry, descent and landing (EDL) on Mars must be large enough to decelerate in a low-density atmosphere and capable of operating in high supersonic flow. Their principle challenge is supersonic deployment. Decelerators for aerocapture deploy in a vacuum, so their associated challenges are different, principally aerothermal and manufacturing with specialized materials.

---

* Chief Engineer, Associate Fellow AIAA.
† Technical Director, Senior Member AIAA.
‡ Senior Engineer.
§ Principal Engineer, Senior Member AIAA.

Inflatable aerocapture decelerators are not necessary for robotic missions to the inner planets and Titan weighing 1 MT or less. However, such devices will eventually become necessary when missions with orbited mass greater than 10 MT are flown. At lighter weights, inflatable aerocapture decelerators will increase payload fraction for outer planet exploration, for heavier Mars and Titan probes, and for Earth-return capsules. At some point the benefit of increased payload fraction, plus the need to push the technology forward for future missions, will overcome the (perceived) risk and (real) cost of advancing the Technology Readiness Level (TRL) of inflatable decelerators, and such devices will be developed and flown.

Less obvious system-level benefits of large deployable decelerators may also include stabilization of otherwise unstable spacecraft and the elimination of the backshell, saving mass and exposing antennae and sensors.

Why do we choose to study, specifically, a Film-Hypercone? A number of concepts/configurations are, or appear, feasible for a deployable aerocapture decelerator. This research focuses on one in particular – a tensile membrane having a conical deployed shape, supported along its rim by an inflatable torus, and constructed of film reinforced by fiber.

Figure 1. Film-Hypercone Inflatable Aerocapture Decelerator.

The reason for choosing the Film-Hypercone for this study is its potential to be the lightest of the known decelerator concepts. We put forward the following arguments in support of this potential:

- Structural Efficiency. The supporting torus is an extremely efficient inflatable structure that is loaded uniformly by membrane tension.
- Minimum Inflation Gas. The inflation gas and associated inflation subsystem components can easily become a large fraction of the decelerator system mass. Hypercone uses the least gas of the known decelerator concepts.
- Thermal Efficiency. The Hypercone configuration with a slender torus maximizes the proportion of decelerator area of thin film that radiates from both surfaces, allowing a higher incident heat flux for a given maximum temperature. The inflatable structure is in a position of relatively low heat flux and is slender so that, if additional thermal protection is needed for the inflatable, it will add little mass.
- Minimum Surface Mass. The relationship between area (BC) as it affects peak temperature, and areal density of known/available materials compatible with those temperatures provides an estimate of the minimum surface mass over a range of ballistic coefficients. This result, from Phase I of this research program, suggest that the minimum mass decelerator use low areal-density film and have a size that is the smallest compatible with the temperature limit of the material.
- Reliability. Other decelerator concepts that rely on multiple inflatable elements will change shape significantly if any one element were to fail or lose pressurization. Because the torus of the Film-Hypercone is slender, it is feasible to add a second, redundant torus such that failure of either one would result in virtually no change in shape.
- Broad Applicability. Finally, it is worth studying a Film-Hypercone because advancement of capabilities related to toroidal inflatable structures will apply to virtually all inflatable aerocapture decelerator concepts.

The object of aerocapture strategies is to insert a spacecraft into an elliptic orbit from a hyperbolic approach trajectory using the destination body's atmosphere to dissipate the excess energy. Although aerocapture may theoretically be accomplished without active control, this requires very accurate targeting and excellent knowledge of the atmosphere. Any practical aerocapture maneuver will require active control of the trajectory. This may be accomplished in two ways: lift modulation or drag modulation. This study uses reference trajectories and heating based on drag modulation, however the feasibility of lifting configurations is studied since there are substantial benefits associated with control by lift modulation.

II. Trajectories

Entry corridors were calculated for aerocapture at Titan and Mars and for drag-modulation and lift-modulation control. These included the effects of ballistic coefficient on the trajectories and the resulting stagnation point heating. For high ballistic coefficients, typical of rigid aeroshells, heat shield mass was estimated for later comparison with inflatable decelerators.

Reference trajectories have been calculated for three ballistic coefficients: 0.5, 0.8 and 1.2 kg/m^2. These are likely to be as high as practical within the capabilities of current materials. The key conditions for 1.2 kg/m^2 are shown in Table 1. The peak acceleration, dynamic pressure, and heating are shown both before and after the

decelerator release since the conditions for the spacecraft may be more severe than those for the inflatable decelerator.

The table shows a large variation in mean free path (MFP) over the trajectory. MFP is small during peak condition, indicating that flow will be in the continuum regime when the decelerator experiences maximum load (maximum dynamic pressure) and maximum surface temperature (peak heat flux). However, it will fly thorough a significant time and distance in rarified gas while entering and exiting the atmosphere, and we must investigate the aerodynamics, stability and aeroelastic effects in these rarified flows.

	Time (s)	Alt (km)	Velocity (km/s)	FPA (deg)	q (Pa)	Accel (m/s^2)	Heat Flux (kW/m^2)	Mean Free Path (m)
Start	0.0	147	6.0	-10.0	0	0.0	0.3	1410
Max Heat Flux	120.6	70	5.4	-2.4	37	28.4	42.5	0.043
Max Deceleration	143.2	66	4.6	-1.5	46	34.6	34.2	0.026
Max q	143.2	66	4.6	-1.5	46	34.6	34.2	0.026
Decelerator Release	168.2	64	3.8	-0.95	40	30.3	21.1	0.019
Max Heat Flux	272.8	60.6	3.8	-0.09	63	0.6	26.1	0.012
Max Deceleration	281.5	60.6	3.8	-0.02	63	0.6	26.1	0.012
Max q	281.5	60.6	3.8	-0.02	63	0.6	26.1	0.012
Min Altitude	287.1	60.6	3.7	0.0	63	0.6	26.0	0.12
150 km	1,072.7	150.0	3.6	3.14	0	0.0	0.0	1227

Table 1. Reference Trajectory – Drag Modulation – Beta = 1.23 kg/m^2.

III. Aerodynamics

We investigated the feasibility of extending closely coupled (dynamic) fluid-structure interaction capability, which now includes a Navier-Stokes solver for continuum flows, to include solvers for free-molecular and transitional flows. We succeeded in coupling a Newtonian solver to LS-DYNA and will, in the future, be able to couple other solvers, assuming expanded computing resources. For rarified flows, we investigated the effect of mean free path on pressure distribution using Direct Simulation Monte Carlo (DSMC) and compared the results to a Newtonian solution. DSMC was also used to calculate pressure and heating distribution for Mars baseline cases.

The pressure distributions on the Hypercone were derived from the DSMC code for a number of different values for the mean free paths (MFP) during the entry into the atmosphere.

Fig. 2 shows the surface pressure distributions over the forward surface of the cone for a range of flow mean free paths. Over the forward part of the cone the pressure distributions look similar for the three values considered. It is interesting to note that the sharp pressure reduction at the corner is absent from the distributions at the larger mean free paths as the flow becomes more rarefied and is less affected by the sharp radius. The most striking feature of the data is the gradual reduction in the effect of the incident shock about halfway along the surface. With an MFP = 0.67 m, the strength of the shock is reduced over that observed at an MFP = 0.06 m, and at an MFP of 6.84 m the effect has completely disappeared. Inspection of the figure shows the corresponding flow pressure distribution and it can be seen that the compression of the flow is now more gradual and diffuse in the flow incident on the cone with no attached shock. The Hypercone is essentially seen as a bluff body by the flow at the larger mean free paths with the diffuse shock standing forward of the entire body.

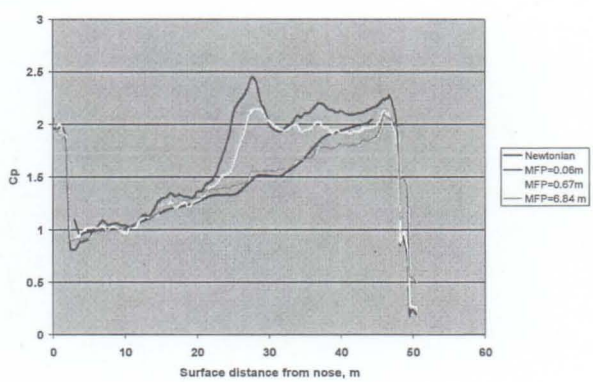

Figure 2. Forward Face Pressure Distributions for Range of Mean Free Paths.

As the angle of the cone surface increases, the pressure gradient within the shock/shear layer increases to a point where the compression waves converge to create a strong detached shock wave ahead of the outer part of the cone. This shock wave is incident on the attached shock layer of the forward part of the cone creating a high-pressure region where the two shock systems converge as can be seen in the flow (Fig. 3), and on the surface distribution in

Fig. 2. Downstream and behind the detached shock the pressure remains relatively constant as it is decelerated due to the relatively large angle between the incident flow and the surface.

Fig. 2 also shows the pressure distribution for a Newtonian flow around the modeled Hypercone geometry. The pressure distribution for the Newtonian flow is modified using a coefficient of 2.1 instead of the value of 2.0 quoted in the majority of the literature as this has been shown to provide a better correlation for bluff bodies. The agreement between the Newtonian solution and the large mean free path output from the DSMC code is very good with the difference between the two falling within 5% of the DSMC value. The distribution for the smaller mean free path simulations show good agreement for the forward and rear part of the cone away from the attached shock location. The Newtonian flow does not accurately model the effect of the concave surface for the flow with the small mean free path.

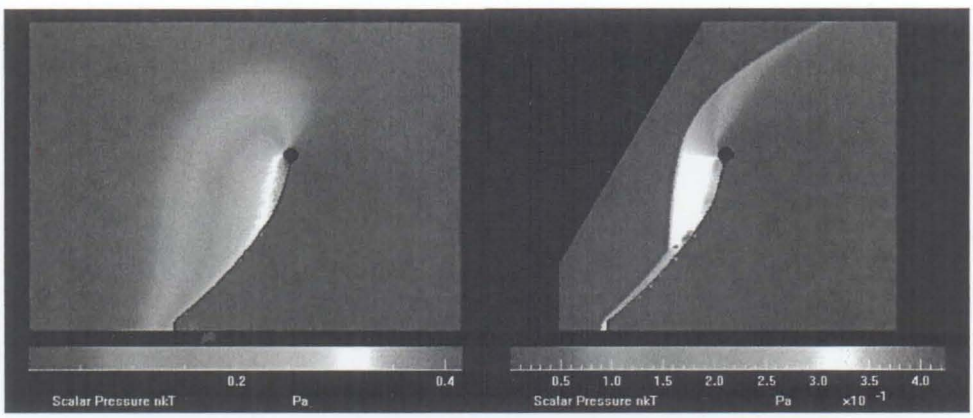

Figure 3. Flow Pressure Distribution, MFP = 6.84 m and MFP = 0.06 m.

The DSMC code also provides the integrated drag of the modeled axi-symmetric body. The data for the three primary flow conditions modeled are presented in Table 2. It can be seen that there is slight trend to increasing drag coefficient with larger mean free paths and this is probably due to the higher average pressure incident on the forward face of the Hypercone as the shock moves away from the surface and out of the shock/shear layer.

MFP (m)	0.06	0.67	6.84
C_D	1.819	1.822	1.956

Table 2. Variation of Drag Coefficient With Flow Mean Free Path.

IV. Fluid-Structure Interaction

Fluid-structure interaction modeling is needed to determine the equilibrium shape and trim incidence of flexible structures in fluid flow. The modeling code LS-DYNA provides a closely coupled dynamic FSI tool for continuum flows using a Navier-Stokes solver. We investigated the feasibility of coupling other CFD solvers for rarified and transitional flows to LS-DYNA.

Closely coupled DSMC analysis of the Hypercone configuration requires significant computer resources. In order to reduce the time, it was decided to create an initial deformed Hypercone geometry and derive an initial pressure distribution using a Newtonian solver. This was considered appropriate due to the high Knudsen number of the flow. This allowed rapid analysis of a number of geometries. The results were subsequently compared with the results of the full DSMC codes for selected cases in order to assess the validity of the Newtonian assumption.

A user-defined routine was created for LS-DYNA to implement a Newtonian flow model. This allows elemental pressures to be derived based on the flow characteristics and the incidence of the element normal to the flow vector. Initial analyses using a DSMC code to simulate the aerodynamics of the Hypercone at representative aerocapture conditions confirmed the suitability of using a Newtonian approximation.

Using the Newtonian routine developed for LS-DYNA, a simulation was run with a fully deformable 80 m Hypercone. Flow conditions at peak dynamic pressure were extracted from the entry simulation output and used to drive the Newtonian model. For a ballistic coefficient of 0.5, corresponding to the 80 m Hypercone configuration, the peak dynamic pressure experienced is 17 Pa. When the pressure distribution is expressed as a pressure

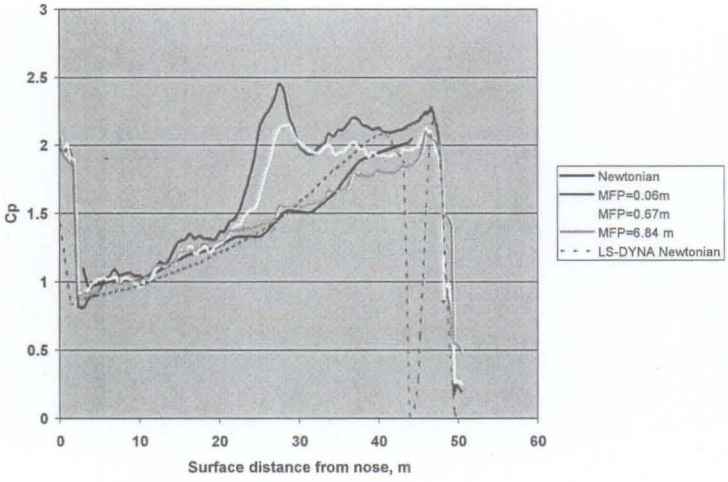

Figure 4. LS-DYNA Newtonian Pressure Coefficient Compared to DSMC Results.

coefficient and plotted with the DSMC and 2-D Newtonian, it can be seen that there is a very close correlation between the results, particularly the 2-D Newtonian and large Mean Free Path DSMC results (Fig. 4). The drop in C_P at 44 m is due to the gap between the edge of the gore and the torus in the more detailed LS-DYNA model not present in the others.

Closely coupled FSI with an efficient Newtonian solver is a potentially useful tool for simulating the decelerator in the rarified gas portion of an aerocapture trajectory. With more extensive computing resources, it will be possible to couple more capable solvers, such as DSMC.

V. Lifting Configurations

Drag modulation, accomplished by cutting-away the decelerator at the point on the trajectory where the desired delta-V has been attained, is the concept that launched interest in inflatable aerocapture decelerators,[1-3] and is the baseline control method for this study. In particular, the mass comparisons that are the key study product are based on drag modulation reference trajectories, and the maximum ballistic coefficient consistent with that trajectory and the material temperature limits. However, if a decelerator could be deployed in a controllable lifting configuration, there are substantial advantages compared to drag modulation. These advantages include lower peak loads and lower peak heating because the trajectory is higher and passes through a lower density portion of the atmosphere. Lower peak heating can be used to increase the ballistic coefficient and, thus, reduce decelerator mass.

The traditional lift modulation method is one in which control is by means of rotating the spacecraft to orient its lift vector.[4] This method of control applies to traditional rigid aeroshells as well as deployable decelerators that are well coupled to the spacecraft and whose moment of inertia is not too large to make roll maneuvering impractical. Our study considered roll-control trajectories and found that an L/D of approximately 0.2 is needed to deal with the combined uncertainties at Mars.

Generation of lift with an inflatable decelerator such as the Hypercone can potentially be achieved through a number of methods. In the simplest case, the inflatable device can be designed with a non-axisymmetric shape, such that, in addition to the dominant drag generated, a lateral force is also produced. Another option is to start with an axisymmetric, conical geometry, then open a vent on one side to induce a lateral force.

The top panel of Fig. 5 shows a notional design in which the gore patterns are adjusted to produce a fixed offset of the spacecraft relative to the center of the torus. This system was modeled using FSI techniques (continuum flow) in which the membrane was free to deflect and the spacecraft and decelerator were free to rotate. The resulting simulation provides the

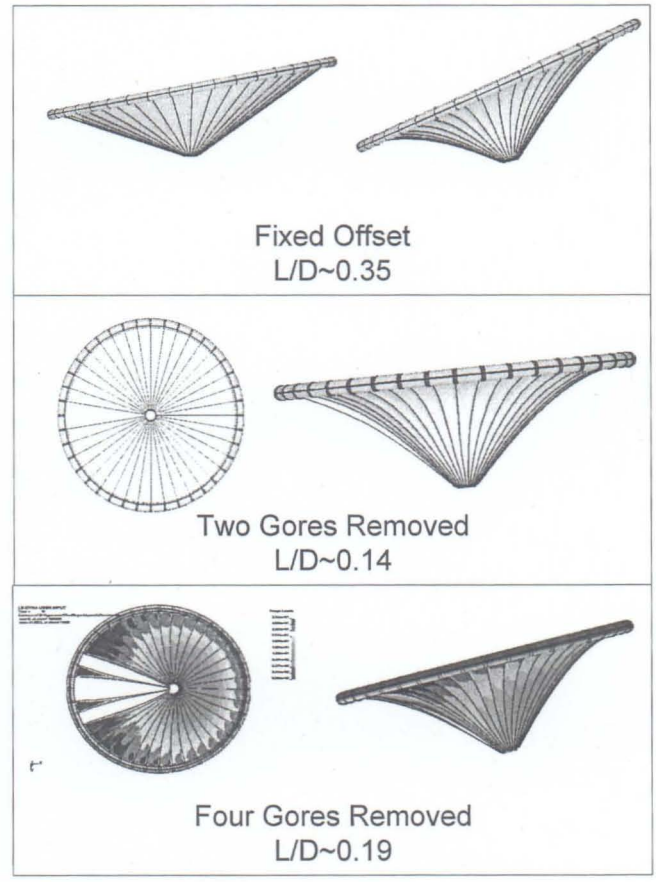

Figure 5. Lifing Configurations.

equilibrium-deflected shape of the decelerator, the trim angle in flight, and a measure of the dynamic stability of the configuration, including aeroelastic modes. The results indicate a trimmed *L/D* of approximately 0.35.

Another approach to inducing the Hypercone to fly at incidence is by venting through gores on one side as shown in the middle panel of Fig. 5. Simulations were performed to investigate the effect of removing two gore panels from the baseline configuration. The figure shows the flying orientation of the vented decelerator, which produced an *L/D* of approximately 0.14.

Since removing two panels provided an *L/D* less than our estimates of that needed for Mars aerocapture, we tried removing an additional two panels as illustrated in the bottom panel of Fig. 5. The result from simulations is an *L/D* of approximately 0.19, which we believe is sufficiently close to the requirement to include this as a feasible approach. Note that removing gore panels reduces drag, such that the overall diameter must be increased somewhat to maintain a particular ballistic coefficient.

The open gore concept suggests another control method in which a zero-lift decelerator is converted to lifting by cutting away gores at a time determined by appropriate control laws. This opens a number of possibilities for mixed control strategies that might be studied in the future.

VI. Thermal Analysis

DSMC has an option that can be selected to calculate convective heat flux to an "adiabatic surface." This is a convenient way to estimate the heat flux and, from the heat flux, surface temperature. However, it is incorrect when applied to aerocapture decelerators with significant backside heat loss. Consider that convective heat transfer, for a given flow, depends on the temperature of the surface, which in turn depends on convective heat flux, requiring an iterative solution. This is performed, presumably, within DSMC for the case of a surface that re-radiates forward, but is insulated in back. Since a Film-Hypercone also rejects heat by radiating from the back surface, DSMC will overestimate the surface temperature and underestimate the convective heat flux if the adiabatic surface option is used. In this research we used an iterative process in which DSMC is used in its "isothermal" mode and multiple runs are made at different assumed surface temperatures in order to more closely estimate surface temperatures and convective heat flux. A typical result of this process is shown in Fig. 6.

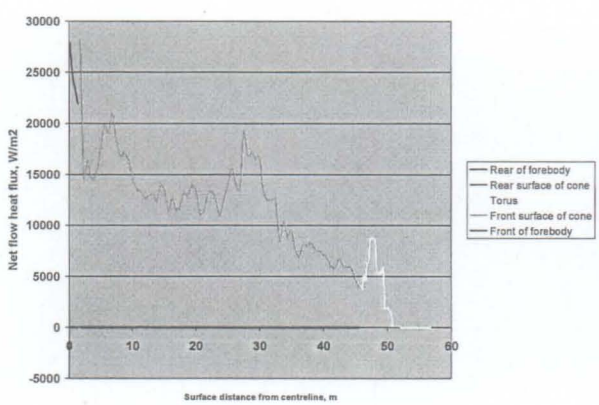

Figure 6. Net Incident Heat Flux Around the Surface of the Hypercone, β=0.5.

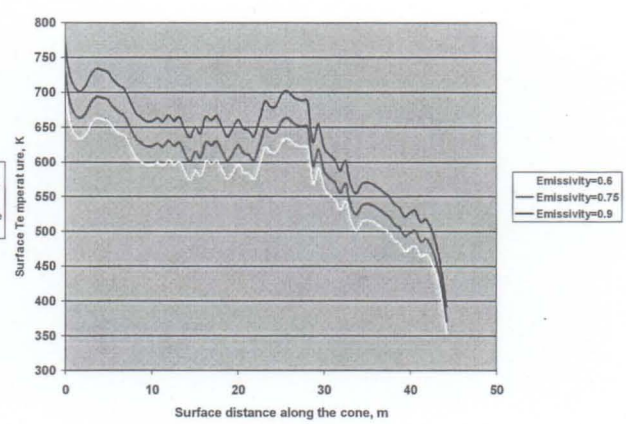

Figure 7. Effect of Cone Surface Emissivity on Material Temperature, β=0.5.

The thermal "mass" of the membrane is so low that it reaches thermal equilibrium with the varying heat flux almost instantaneously. However, the inflated torus shows some thermal lag as the gas heats up and convective processes transfer heat to the aft surface. We developed a thermal model for this process that is not reported here since it does not change any global results, but will be an important consideration in future detailed designs for flight.

The results of the heat transfer calculations to determine equilibrium surface temperatures are shown in Fig. 7 for a range of material emissivity. With the cone made of Kapton with an assumed maximum temperature of 500 °C (773 K) the temperature is just within the specifications of the material and, therefore, 0.6 is the minimum value of emissivity that the cone material should exhibit. Increasing the emissivity by the application of an appropriate

coating or surface preparation will help increase the temperature margin on the cone material as seen in the comparative temperature plots of the chart.

The effect of an increase in the ballistic coefficient on the peak heating experienced on the cone surface is not easily predicted. Therefore a number of DSMC runs were carried out for a series of similar Hypercone geometries over a range of ballistic coefficients. It was assumed that the deformed shape of the Hypercone was the same for the range of ballistic coefficients analyzed and that the torus diameter scaled with the overall diameter.

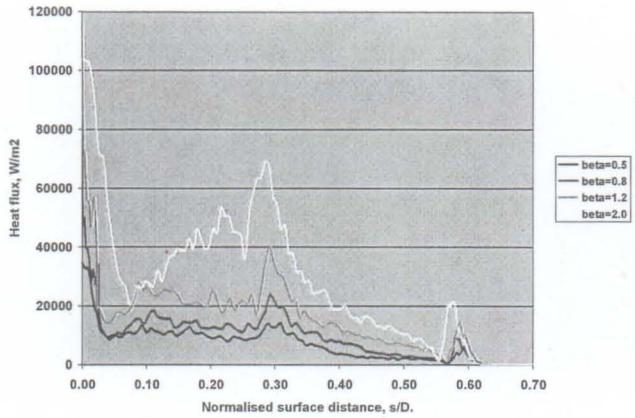

Figure 8. Variation of Incident Heat Flux with Ballistic Coefficient.

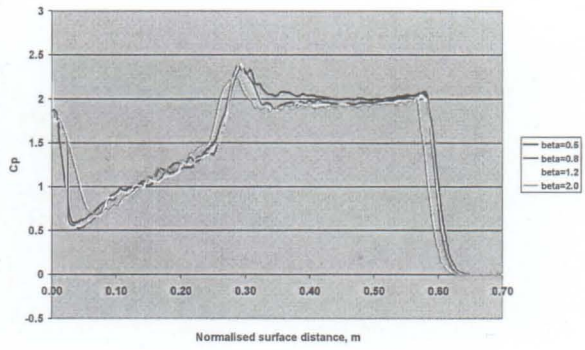

Figure 9. Pressure Distribution on the Forward Face of the Hypercone.

Fig. 8 shows the heat flux distributions over the forward face of the Hypercone for the various ballistic coefficients. The flow conditions corresponding to the expected peak heating conditions on the trajectories for the various configurations are presented in Table 3 along with the basic geometries of each configuration. As expected, the peak heating for each of the configurations occurs at a lower altitude for increasing ballistic coefficient as indicated by the free stream density. Each of the flow conditions exhibits similar free stream velocity and therefore flow enthalpies, however the increase in density for the flow conditions results in higher enthalpy flux within the shear layers and consequently overall higher levels of heat transfer to the surface as indicated in the chart.

Ballistic Coefficient, kg/m^2	0.5	0.8	1.2	2.0
Overall Diameter (D), m	83.5	66.0	53.9	41.75
Torus Diameter, m	3.5	2.77	2.26	1.75
MFP, m	0.06	0.044	0.028	0.015
V, m/s	5,312	5,244	5,241	5,295
ρ, kg/m^3	1.274×10^{-6}	1.764×10^{-6}	2.790×10^{-6}	5.136×10^{-6}

Table 3. Geometry and Peak Heating Flow Conditions for DSMC Simulations.

While the inviscid flow is unaffected by the scale of the body, the development of the shear layers is dependent on the stream length. The pressure coefficient at the shock location in each case is essentially the same as shown in Fig. 10. Therefore for the smaller geometries the stream length from the nose to the shock location is shorter, which produces a stronger adverse pressure gradient. The stronger adverse pressure gradient will cause the shear layer to thicken more rapidly thereby producing a relatively thicker shear layer at the shock location for the high ballistic coefficient Hypercones. The increased frictional dissipation in this thicker shear layer produces increased heating of the surface as seen in the figure. At the shock location the shear layer is thinned considerably due to the increase in pressure imposed by the strong shock wave. This thinning of the boundary layer greatly increases the heat transfer between the flow and the surface causing the peaks in the profiles seen at the normalized distance of 0.3. The strong adverse pressure gradient associated with the shock may also induce the shear layer to separate just upstream of the shock. In this region the surface is "protected" from the heating in the shear layer by the separated flow and this may explain the sharp decrease in incident flux just before the peak associated with the shock on some of the traces.

Processing of the heat fluxes determined from the constant wall temperature DSMC runs as described at the start of this section for each of the ballistic coefficients yields the temperature distributions shown in Fig. 10. As expected, the surface temperatures increase with increasing ballistic coefficient at all points along the cone, but they are particularly high in the region of the secondary shock impingement. Examination of the temperatures reveals that the maximum ballistic coefficient that can be flown, while respecting the assumed maximum service temperature of the Kapton material of approximately 770 K, is 1.2, with the maximum temperature attained at the shock location being 767 K assuming a surface emissivity of 0.9.

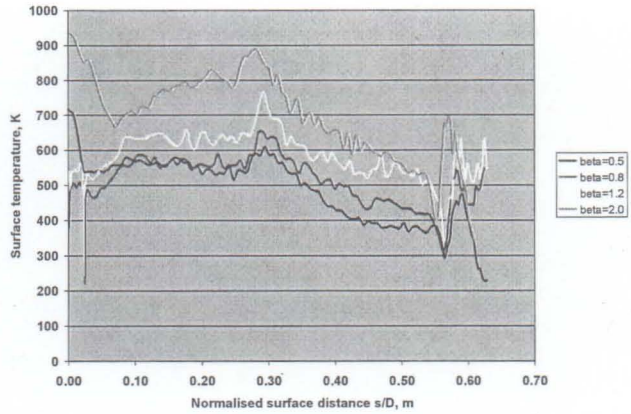

Figure 10. Variation in Cone Surface Temperature with Ballistic Coefficient at Peak Heating Conditions.

VII. Cone Angle

A potentially significant disadvantage of the Hypercone configurations is the secondary heating peak we note at approximately $s/D = 0.3$. This second peak is a consequence of the concave natural shape of the tensile membrane under pressure loading, and the resulting shock interaction with the surface. We would prefer a monotonically decreasing heat flux on the membrane surface, maintaining some small fraction of stagnation heat flux.

The potential for improved heating distribution was investigated by variation of the cone angle while maintaining a ballistic coefficient of 1.2. Again, DSMC runs were performed on the deformed geometries of 45° and 65° Hypercones for comparison with the 55° geometry analyzed thus far. The geometry input for each of the cases was simple arc approximations to the shape derived from LS-DYNA runs.

Fig. 11 shows the heat flux distributions for the three cone angles with the surface distance normalized with the total distance from the nose to the center of the rear face. It can be seen that the 45° Hypercone exhibits lower fluxes on the forward face upstream of the shock location as a result of a thinner shear layer produced by the less adverse pressure gradient. However, the lower cone angle produces a stronger shock wave as a result of the lower pressure and therefore higher local Mach number. The thin shear layer coupled with the higher temperatures in the shock produce a very high peak in the heat transfer at the shock location when compared with the 55° Hypercone. Clearly the higher mass associated with the 45° Hypercone coupled with the very high flux at the shock location does not show any advantage over the 55° configuration.

The heat flux data for the 65° Hypercone shown in Fig. 11 reveals the removal of the peak associated

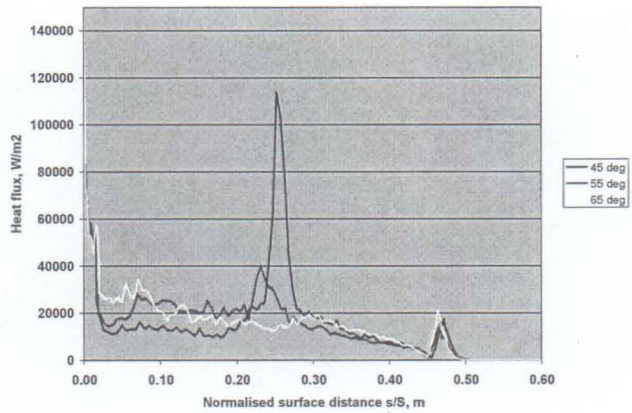

Figure 11. Forward Face Incident Heat Fluxes for Hypercones of Various Angles.

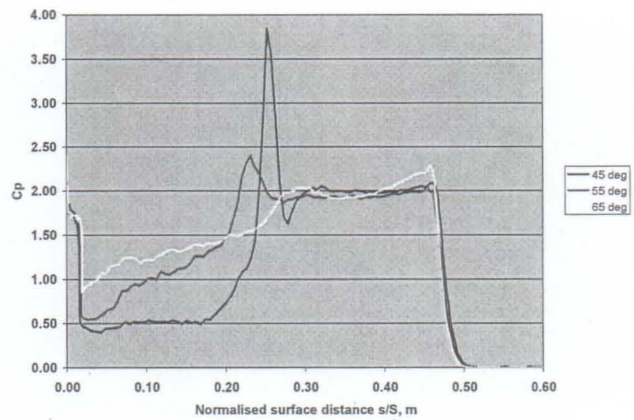

Figure 12. Pressure Distributions for Different Cone Angles, $\beta = 1.2$.

with the shock location. This is confirmed by the pressure distribution of Fig. 12. Inspection of the flow field as seen in Fig. 13 shows that the attached shock within the shear layer begins to move away from the surface of the Hypercone as the surface angle increases and shows the characteristics of the flow around a bluff body. This stronger shock within a thickening shear layer explains the initially higher flux close to the leading edge of the cone; however, as the shock moves away from the surface, the source of heat within the shear layer is dispersed and the level of the flux falls. The base of the main incident shock is held off from the wall and is also dispersed by the presence of the detaching surface shock with further insulation of the surface by the cooler and thick shear layer resulting in the significantly lower surface heat transfer at the shock location.

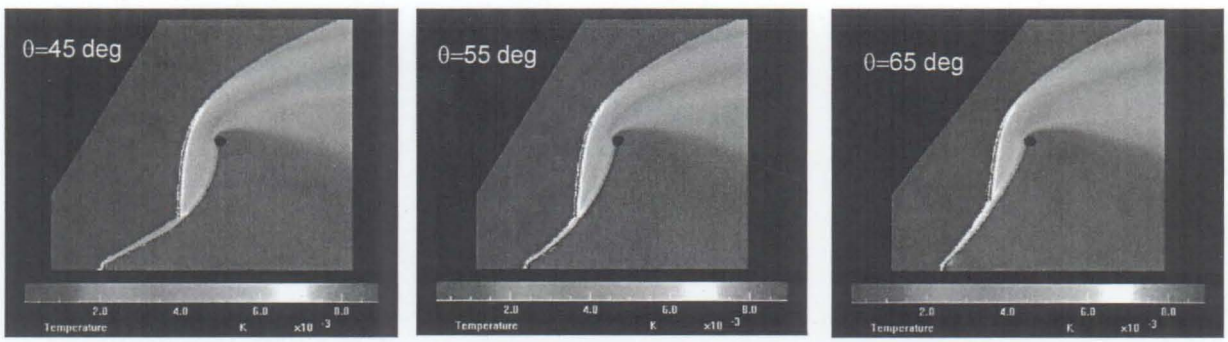

Figure 13. Flow Field Temperature at Various Cone Angles.

The results suggest that the 65° Hypercone could have a mass advantage due to the reduced heating compared to the 55° Hypercone and that a higher ballistic coefficient could be flown within the current maximum assumed surface temperature. However, analysis carried out in a previous study[5] highlighted that, from a purely structural perspective, 55° was the lowest mass configuration for a given dynamic pressure. Further investigations for this application are required to establish the optimum cone angle from both a structural and aerothermal perspective.

VIII. Manufacturing Technology

The Hypercone is an aerodynamic deceleration device comprising a flexible conical membrane attached to an entry vehicle at the nose, and supported at the base by an inflatable torus (Fig. 14). The cone is constructed from a number of gores, with thicker radial seams forming the principal load path through the device. The torus is a circular cross-section inflatable membrane, with stiffening straps running around the major circumference to improve buckling resistance. The radial seams of the cone attach to the torus through loops running around the minor circumference of the torus.

This section summarizes manufacturing technology developed for lightweight inflatable toroidal structures relevant for most inflatable aerocapture decelerator concepts (not just Hypercone). Fig. 15 shows several examples of inflatable decelerator concepts found in the open literature that include one or more inflatable tori.

We developed a method for cold-forming Kapton

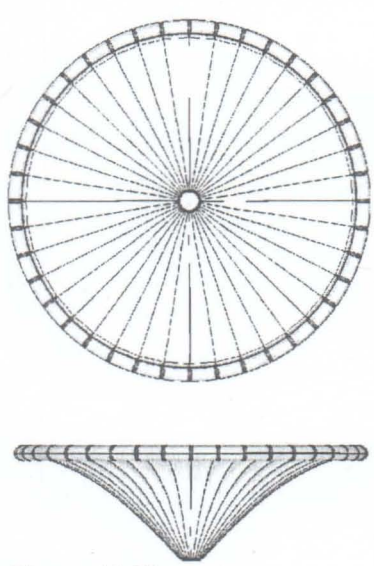

Figure 14. Hypercone Configuration.

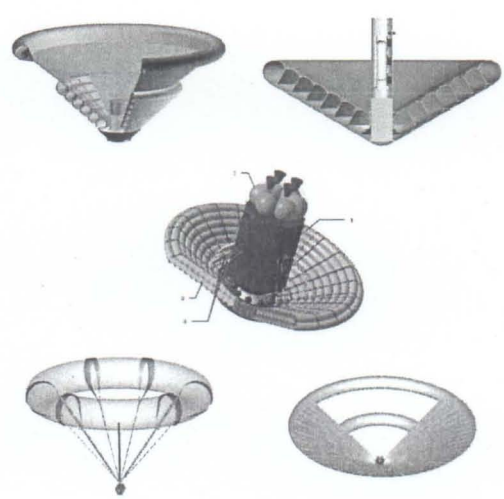

Figure 15. Aerocapture Decelerator Concepts with Toroidal Structures.

film as a part of a manufacturing method for fiber-reinforced tori. Room-temperature processes were used in order to ensure that the process would be scalable to very large structures. A 10-m diameter torus was constructed and tested.

We also wanted to demonstrate the ability to provide fiber reinforcement of the film. In an earlier study[6] we found that for a 12× advantage in specific strength of fiber compared to film, an example structure had a 7× lower mass, with adhesives, seams, and the non-structural gas barrier film taken into account. The reinforced structure is not only lighter, but it has high bending stiffness, important for stability in compression, and does not rely on seam adhesive strength at high temperature.

The manufacturing technologies explored during Phase II of this research program included characterizing Kapton film elongation and permanent deformation, curved Kapton bladder fabrication techniques, extremely light weight open architecture Vectran braid fabrication, and Kapton/braid bonding methods.

Elongation tests were performed on 0.001-in thick Kapton samples to determine the permanent deformation. These pull-test coupons were tested in a Thwing-Albert materials pull test machine. Elongations of 15 to 20% yielded permanent deformations of 2 to 3%, adequate for fabrication of this prototype.

Fabrication techniques were developed through sub-scale and full-scale curved beam test articles, and adhesive and tape bonding tests. Fabrication tooling was built to support this process development.

The results of these investigations yielded a 10-m (33-ft) inner diameter torus assembly of 10-in cross-section. The completed assembly weighs 2.4 kg, including one metal Schrader valve inlet port.

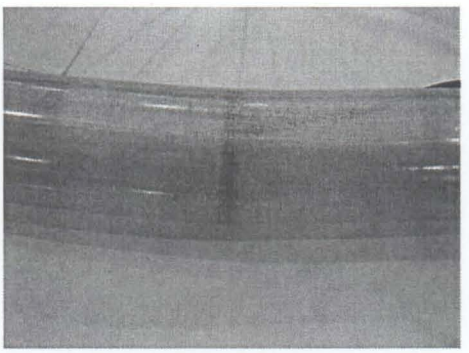

Figure 16. Section Joint with Seam and Overlapping Fiber Reinforcement.

The bladder was fabricated in quarter sections from Kapton bonded with silicone transfer adhesive and Kapton tape. The structural braid was constructed of Vectran fibers. The first quarter-section bladder/braid assembly was built for developing the braid to Kapton bond, strap application techniques, and pressure testing. This quarter-section assembly was proof-test pressurized to 10 psi without failure.

The torus assembly has an inner and two outer straps of 0.20-in wide 760-lb Vectran tape bonded to the formed Kapton/braid assembly. The inner strap sets the inner diameter and carries the axial tension loads. The outer straps are set 90° to each other (45° either side of the horizontal centerline) and provide planar stiffness. By selecting the strap construction and their location on the section, bending stiffness (EI) can be tailored independently for in-plane and out-of-plane bending.

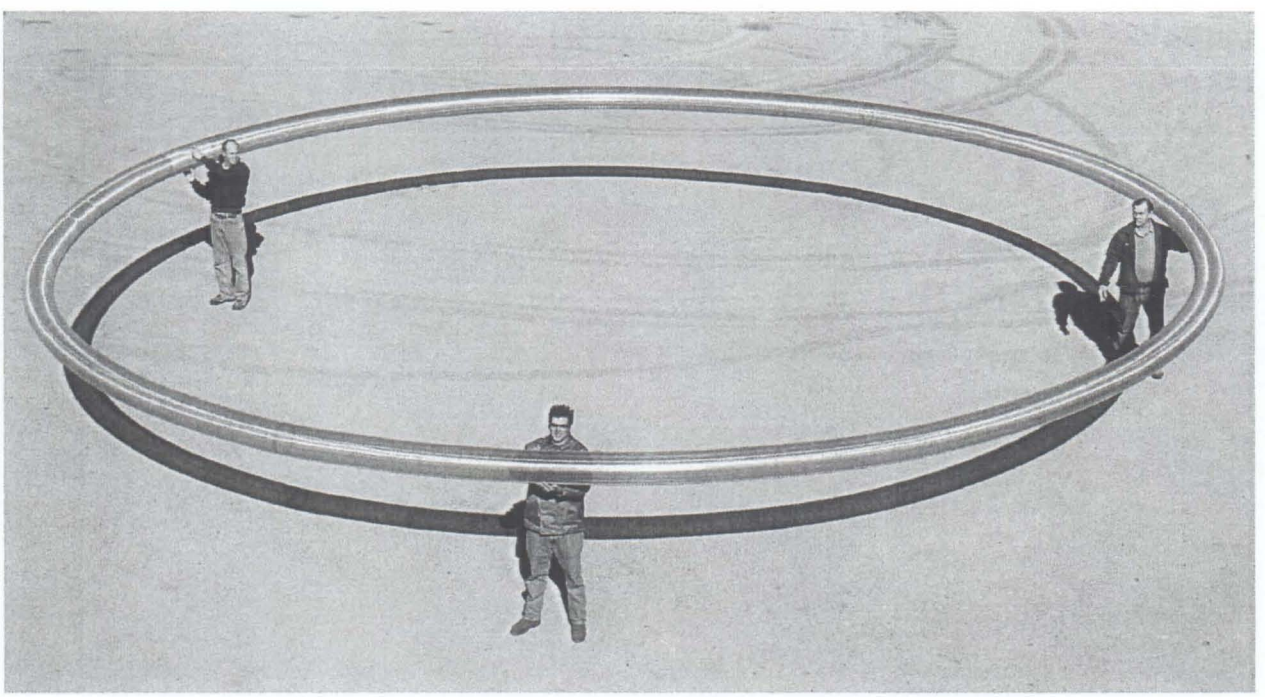

Figure 17. Finished 10-m Torus.

The innovative manufacturing techniques of stretch-forming thin Kapton film and the development of extremely lightweight stabilized Vectran braid led to the fabrication of a proof-of-concept toroidal airbeam. This airbeam torus shows that a Hypercone-type decelerator assembly can be built from high-temperature, low-elongation materials with extremely low inflated densities and high planar stiffness.

IX. Mass Comparisons

The Mars baseline cases of 1.5, 2.0, and 5.0-MT orbited mass were used to estimate the mass of inflatable aerocapture decelerators. Comparisons were made between a rigid aeroshell, inflatable stressed-film decelerators with a 500 °C surface temperature limit, and fiber-reinforced film decelerators, also with a 500 °C limit. Our analysis shows that fiber reinforcement over a thin film saves considerable mass compared to either a stressed-film inflatable or a rigid aeroshell.

Reference trajectories have been constructed for aerocapture events using three ballistic coefficients: 30, 50, and 100 kg/m^2. For each one, the required thickness of TPS has been calculated (assuming the material properties for a typical low-density ablator) and the total spacecraft mass for payload masses of 1,500 and 2,000 kg. These are shown in Table 4.

Payload Mass (kg)	1,500	1,500	1,500	2,000	2,000	2,000	5,000	5,000	5,000
Ballistic Coefficient (kg/m^2)	30	50	100	30	50	100	30	50	100
Heat Shield Diameter (m)	10.5	7.3	4.8	12.2	8.4	5.5	19.2	13.3	8.7
TPS Thickness (mm)	14	16	19	14	16	19	14	16	19
TPS Mass (kg)	624	339	172	832	452	229	2,081	1,130	573
Heat Shield Mass (kg)	1,120	574	272	1,492	765	363	3,730	1,913	908
Overall Spacecraft Mass (kg)	2,620	2,074	1,772	3,492	2,765	2,363	8,730	6,913	5,908
Heat Shield Mass Fraction	43%	28%	15%	43%	28%	15%	43%	28%	15%

Table 4. Masses of Conventional, Rigid-Aeroshell Aerocapture Vehicles.

Payload Mass (kg)	1,500	2,000	5,000
Hypercone Diameter (m)	30	34	53.5
Torus Diameter (m)	1.7	2	3
Inflation Pressure (Pa)	7,400	7,400	7,400
Inflation Gas Mass (kg)	6.5	10.2	36
Inflator Mass (kg)	6.5	10.2	36
Torus Thickness (μm)	125	125	175
Torus Mass (kg)	93.2	124.3	407.5
Strap Mass (kg)	3.6	5.1	20.8
Attachment Loop Mass (kg)	0.39	0.6	2.23
Radial Seam Mass (kg)	1.1	1.6	6.7
Gore Thickness (μm)	200 & 125	200 & 125	200 & 125
Gore Mass (kg)	142.3	182	452.9
Total Hypercone Mass (kg)	**253.6**	**334.0**	**962.1**
Overall Spacecraft Mass (kg)	**1,753.6**	**2,334.0**	**5,962.1**
Ballistic Coefficient	1.19	1.23	1.26
Hypercone Mass Fraction	**14%**	**14%**	**16%**

Table 5. Hypercone Dimensions and Mass Breakdown for Un-reinforced Polyimide Film Construction Material, BC ≈ 1.2.

Payload Mass (kg)	1,500	2,000	5,000
Hypercone Diameter (m)	30	34	53.5
Torus Diameter (m)	1.7	2	3
Inflation Pressure (Pa)	7400	7400	7400
Inflation Gas Mass (kg)	6.5	10.2	36
Inflator Mass (kg)	6.5	10.2	36
Torus Braid Mass (kg)	8.7	13.6	48
Torus Film Mass (7.5μm Upilex) (kg)	5.5	7.4	17.5
Strap Mass (kg)	3.6	5.1	20.8
Attachment Loop Mass (kg)	0.39	0.6	2.23
Radial Seam Mass (kg)	1.1	1.6	6.7
Gore Braid Mass (kg)	26.6	34.1	85.9
Gore Film Mass (7.5μm Upilex) (kg)	8.3	10.6	26.8
Total Hypercone Mass (kg)	**67.2**	**93.4**	**279.9**
Overall Spacecraft Mass (kg)	**1,567.2**	**2,093.4**	**5,279.9**
Ballistic Coefficient	1.07	1.11	1.12
Hypercone Mass Fraction	**4%**	**4%**	**5%**

Table 6. Hypercone Dimensions and Mass Breakdown, Film with Fiber Overbraid, BC ≈ 1.2.

It can be seen that the mass fraction represented by the heat shield increases significantly as the ballistic coefficient decreases. The limiting ballistic coefficient for a stable blunted cone configuration is about 100 kg/m^2, which results in a heat shield mass of approximately 15% of the overall spacecraft mass. It should be noted that the heat shield diameters required to achieve the lower ballistic coefficients are not compatible with launch from current expendable launch vehicles with launch fairing diameter no larger than 5 m. The 2,000 kg payload mass is, therefore, close to the limit which may be delivered using current technology. The 5,000 kg payload would require a large aeroshell assembled in Earth orbit.

With the revised geometry and stress data fed into the mass model, final system mass estimates were generated for Hypercones with a ballistic coefficient of around 1.2. Table 5 shows the projected masses for Hypercones constructed purely from polyimide film. Table 6 shows the comparative system mass breakdown for a minimum thickness Film-Hypercone, with a high tenacity fiber overbraid. The projected system mass is less than a third of the equivalent Upilex-alone mass, giving a mass fraction of only 4%. This uses readily available materials and technology.

X. Conclusion

A drag-modulated fiber-reinforced Film-Hypercone with a surface temperature limit of 500 °C is feasible for a 5 MT Mars orbiter and will have a mass fraction of approximately 5%. Without fiber reinforcement (relying on film strength alone) the mass fraction is 16%.

A number of Hypercone-based configurations are capable of generating lift. A lift-modulated decelerator of this type will experience lower peak heating than a drag-modulated decelerator with the same ballistic coefficient. Similarly, a 65° Hypercone will have lower peak heating on the deployed surface than a similar configuration with lower cone angles. Either of these enhancements would lead to a design lighter than the baseline example.

A Film-Hypercone is currently the lightest decelerator concept using available materials. However, these results are extremely sensitive to material temperature limits. Higher temperature fiber/fabric technology would have a high potential for lighter, more robust aerocapture decelerators. More research is needed on tailored materials for this application. No other research investment will have a higher payoff in this field.

Acknowledgments

The work described in this paper was funded in whole or in part by the In-Space Propulsion Technologies Program, which is managed by NASA's Science Mission Directorate in Washington, DC, and implemented by the In-Space Propulsion Technology Office at Marshall Space Flight Center in Huntsville, Alabama. The program objective is to develop in-space propulsion technologies that can enable or benefit near and mid-term NASA space science missions by significantly reducing cost, mass, and travel times.

This research was performed under a Small Business Innovation Research grant. The support of Bonnie James and Erin Richardson at Marshall Space Flight Center is gratefully acknowledged.

The work of Michael Quinn and Paul Anderson, under the direction of Lynn Fogleman at Vertigo, in developing innovative methods for manufacturing lightweight membrane structures is also acknowledged.

References

[1]Hall, J.L., and Le, A.K., "Aerocapture Trajectories for Spacecraft with Large, Towed Ballutes," AAS 01-235, Washington, DC, 2001.

[2]Hall, J.L., "A Review of Ballute Technology for Planetary Aerocapture," *AIAA Meeting Papers on Disc* [CD-ROM], AIAA-2000-0382, Reston, VA, 2000.

[3]McRonald, A., "A Light-Weight Hypersonic Inflatable Drag Device for a Neptune Orbiter," AAS 00-170, Washington, D.C., 2000.

[4]Cerimele, C.J., and Gamble, J.D., "A Simplified Guidance Algorithm for Lifting Aeroassist Orbital Transfer Vehicles," AIAA-85-0348, Reston, VA, 1985.

[5]Brown, G., Epp, C., Graves, C., Lingard, S., Darley, M., and Jordan, K., "Hypercone Inflatable Supersonic Decelerator," *AIAA Meeting Papers on Disc* [CD-ROM], AIAA-2003-2167, Reston, VA, 2003.

[6]Brown, G.J., " Inflatable Structures for Deployable Aerocapture Decelerators," Proceedings of JANNAF Conference, 2005.